AGU PUBLICATIONS

JGR

Journal of Geophysical Research: Space Physics

RESEARCH ARTICLE
10.1002/2017JA024295

Key Points:
- Two hundred forty-eight flux ropes identified in Mercury's magnetotail (74 cylindrical and linearly force-free)
- Flux ropes most commonly observed by MESSENGER postmidnight, moving planetward
- Flux ropes observed intermittently, but most often when the preceding lobe field is enhanced

Correspondence to:
A. W. Smith,
aw.smith@soton.ac.uk

Citation:
Smith, A. W., J. A. Slavin, C. M. Jackman, G.-K. Poh, and R. C. Fear (2017), Flux ropes in the Hermean magnetotail: Distribution, properties, and formation, *J. Geophys. Res. Space Physics*, *122*, doi:10.1002/2017JA024295.

Received 25 APR 2017
Accepted 17 JUL 2017
Accepted article online 20 JUL 2017

Flux ropes in the Hermean magnetotail: Distribution, properties, and formation

A. W. Smith[1], J. A. Slavin[2], C. M. Jackman[1], G.-K. Poh[2], and R. C. Fear[1]

[1]Department of Physics and Astronomy, University of Southampton, Southampton, UK, [2]Climate and Space Sciences and Engineering, University of Michigan, Ann Arbor, Michigan, USA

Abstract An automated method was applied to identify magnetotail flux rope encounters in MESSENGER (MErcury Surface, Space ENvironment, GEochemistry, and Ranging) magnetometer data. The method identified significant deflections of the north-south component of the magnetic field coincident with enhancements in the total field or dawn-dusk component. Two hundred forty-eight flux ropes are identified that possess well-defined minimum variance analysis (MVA) coordinate systems, with clear rotations of the field. Approximately 30% can be well approximated by the cylindrically symmetric, linearly force-free model. Flux ropes are most common moving planetward, in the postmidnight sector. Observations are intermittent, with the majority (61%) of plasma sheet passages yielding no flux ropes; however, the peak rate of flux ropes during a reconnection episode is ~5 min^{-1}. Overall, the peak postmidnight rate is ~0.25 min^{-1}. Only 25% of flux ropes are observed in isolation. The radius of flux ropes is comparable to the ion inertial length within Mercury's magnetotail plasma sheet. No clear statistical separation is observed between tailward and planetward moving flux ropes, suggesting the near-Mercury neutral line (NMNL) is highly variable. Flux ropes are more likely to be observed if the preceding lobe field is enhanced over background levels. A very weak correlation is observed between the flux rope core field and the preceding lobe field orientation; a stronger relationship is found with the orientation of the field within the plasma sheet. The core field strength measured is ~6 times stronger than the local dawn-dusk plasma sheet magnetic field.

1. Introduction

The flybys of Mercury by the Mariner 10 and MESSENGER (MErcury Surface, Space ENvironment, GEochemistry, and Ranging) spacecraft demonstrated that Mercury possesses an internal magnetic field, one with the same polarity as Earth's field and a magnetic dipole moment of 195 ± 10 nT R_M^3 (where R_M is the radius of Mercury: 2440 km) [*Ness et al.*, 1974; *Anderson et al.*, 2012]. Mercury's field is approximately aligned with its spin axis but offset north from the planetary center by approximately $0.2R_M$ [*Alexeev et al.*, 2008, 2010; *Anderson et al.*, 2008, 2010, 2011; *Johnson et al.*, 2012].

At the orbit of Mercury, by conservation of mass and magnetic flux, the solar wind is found to be ~5–10 times denser and coupled with an interplanetary magnetic field (IMF) ~3–6 times stronger than is observed at Earth [*Burlaga*, 2001]. The combination of its weak internal field (approximately 1% the strength of Earth's field) and an average distance to the Sun of only ~0.38 AU results in one of the most extreme magnetospheres found in the solar system; one that can vary on the timescale of minutes [*Slavin et al.*, 2010; *Sun et al.*, 2015]. The strong solar wind conditions and relatively small internal magnetic field contribute to create a very compact magnetosphere, with an average magnetopause standoff distance of only ~1.45 R_M [*Ness et al.*, 1976; *Winslow et al.*, 2013; *Zhong et al.*, 2015]. Furthermore, during extreme solar wind dynamic events the magnetopause standoff distance has been observed to decrease to 1.03–1.12 R_M, just above the planetary surface [*Slavin et al.*, 2014].

The process of reconnection is critical to understanding the large-scale dynamics of Mercury's magnetosphere. It is the fundamental process by which magnetic fields can reconfigure, changing the local magnetic topology and transferring energy from the field to the local plasma. On the dayside of a planet, reconnection can occur between the IMF and the planet's internal field. Here reconnection results in the transfer of mass, momentum, and energy from the solar wind into the magnetosphere. Once the magnetospheric field lines are connected into the solar wind (they are open), they can convect toward the nightside of the planet over

the magnetic poles, with the ambient solar wind flow, to form the magnetotail lobes. The open field lines in the lobes sink toward the center of the magnetotail and reconnect once more, closing the magnetospheric field. The convection of the recently closed field lines around the dawn and dusk flanks completes what is known as the Dungey cycle [*Dungey*, 1961]. At Earth, the timescale for the Dungey cycle, the time between the field lines being opened on the dayside and their subsequent closure on the nightside, is of the order of 1 h [*Cowley*, 1981; *Browett et al.*, 2017]. In contrast, the timescale at Mercury is thought to be as little as ~2 min [*Siscoe et al.*, 1975; *Christon*, 1987; *Slavin et al.*, 2009, 2012].

During episodes of magnetotail reconnection the quasi antiparallel fields on either side of the magnetotail current sheet come together and reconfigure. If this happens at a single location in the magnetotail, then it might be expected that on the planetward side of the reconnection site, the newly closed but stretched field lines will evolve under magnetic tension and return to a more dipole-like configuration (known as a dipolarization). On the far side of the reconnection site, the open field lines, those connected at both ends to the IMF, will be expelled down the magnetotail into the solar wind.

The picture changes somewhat if reconnection occurs at two or more locations. In a simplified, two-dimensional picture this scenario results in the formation of magnetic islands (or plasmoids) between the sites of reconnection [*Schindler*, 1974; *Hones*, 1977; *Eastwood and Kiehas*, 2015]. Moving to a three-dimensional scenario, the magnetic islands (or loop-like plasmoids) will be formed only if there is no magnetic shear across the magnetotail current sheet: the fields are perfectly antiparallel. At Earth it is commonly observed that there is an azimuthal component, or shear across the magnetotail caused by the influence of the solar wind [*Fairfield*, 1979; *Cowley*, 1981]. The azimuthal field across the magnetotail can act as a guide field during reconnection, resulting in the creation of flux rope-type plasmoids, possessing a helical topology with a strong core axial field [*Hughes and Sibeck*, 1987; *Moldwin and Hughes*, 1991]. Indeed, *Moldwin and Hughes* [1992] found a strong correlation between the dawn-dusk component of the magnetic field present within magnetotail flux ropes and the magnitude and direction of preceding IMF: in 88% of their events the azimuthal field in the flux rope was found to be in the same direction as the IMF (when averaged over the previous hour). *Slavin et al.* [2003] found a similar result, with 79% of their 28 flux ropes found to be consistent with the preceding IMF. However, a more recent study of 27 terrestrial flux ropes found only a weak correlation [*Borg et al.*, 2012] and identified events with opposing polarities within the same reconnection burst. *Teh et al.* [2014] attributed this discrepancy to be a result of the relative strength of the guide field (B_G); only strong guide fields (greater than 20% of the reconnecting field) were found to result in core fields consistent with the external field. For weak B_G the flux rope core polarity more closely matched the quadrupolar Hall magnetic field. This is still an active area of research.

If the rate of reconnection on the magnetopause is larger than that found within the magnetotail, then the magnetotail will become loaded with magnetic flux (and energy). This flux can be later dissipated in episodes of substorm-like activity [*Siscoe et al.*, 1975; *Slavin et al.*, 2010, 2012; *Sun et al.*, 2015], much like at the Earth [*Akasofu*, 1964; *Baker et al.*, 1996; *Huang*, 2002].

Evidence for reconnection-driven magnetotail dynamics at Mercury were first identified in the energetic particle data obtained during the Mariner 10 flybys [*Baker et al.*, 1986; *Eraker and Simpson*, 1986]. More recently, analysis of the MESSENGER magnetometer data has revealed many in situ encounters with dipolarizations [*Sundberg et al.*, 2012; *Sun et al.*, 2016] and flux ropes [*Slavin et al.*, 2009, 2012; *Di Braccio et al.*, 2015; *Sun et al.*, 2016] within the Hermean magnetotail.

The dominant direction of motion of flux ropes in the magnetotail is determined by the location of the near-Mercury neutral line (NMNL) relative to the flux rope. Flux ropes formed on the sunward side of the NMNL will move toward the planet and are thought to undergo rereconnection with the strong dipole field close to the planet [*Slavin et al.*, 2003]. Conversely, flux ropes tailward of the NMNL move down the magnetotail and are ejected into the solar wind [cf. *Hones et al.*, 1984; *Moldwin and Hughes*, 1992; *Ieda et al.*, 1998]. From energetic particle data collected during the Mariner 10 flyby, *Baker et al.* [1986] concluded that the NMNL was located between 3 and 6 R_M down the Hermean tail. Following this, evidence from the MESSENGER M2 and M3 flybys determined the location of the neutral line (during these flybys) to be 2.8 R_M and 1.8 R_M from the planet, respectively [*Slavin et al.*, 2012]. The vicinity of the NMNL (~1–3 R_M) was later well sampled by MESSENGER's orbital phase; a survey of which agreed the location of the NMNL to be approximately 2–3 R_M downtail [*Di Braccio et al.*, 2015]. More recently, *Poh et al.* [2017] performed a statistical analysis, using the sign of the B_Z

component of the magnetic field to infer the relative location of MESSENGER and concluded that the NMNL is statistically located 3 R_M down the Hermean tail.

The aim of this study is to investigate flux ropes in the Hermean magnetotail, with particular focus on their properties, location, and formation. We present the most comprehensive survey of MESSENGER magnetometer data, identifying 248 flux ropes. Of these, 74 are confirmed to be well represented by a cylindrical, linearly force-free flux rope model.

Section 2 will introduce the data used, the magnetic field signatures of interest, and the flux rope magnetic field model utilized. The method will be briefly summarized in section 3. The results of this survey will then be explored with respect to the location, recurrence, and motion of the flux ropes. Finally, the structures will be discussed with a focus on their formation and the driving of the Hermean magnetotail.

2. Data, Signatures, and Models

This section will summarize the data utilized by the study, as well as the signatures of interest and relevant magnetic field models.

2.1. Data

The MESSENGER spacecraft [*Solomon et al.*, 2007] orbited Mercury for ~4 years between March 2011 and April 2015. This study utilizes data obtained during this interval from the onboard magnetometer [*Anderson et al.*, 2007]. Data are used at a sampling rate of 20 Hz; use of such a high time resolution is necessitated by the short timescales at Mercury; previous work found that flux rope encounters at Mercury generally last for less than 3 s [*Slavin et al.*, 2012; *Di Braccio et al.*, 2015].

The magnetic field data in this study have been used in the Mercury Solar Magnetospheric (MSM) coordinate system. In this Cartesian system the $\hat{X}_{MSM}$ axis is directed sunward, the $\hat{Z}_{MSM}$ axis is directed northward along the magnetic dipole axis, and the $\hat{Y}_{MSM}$ axis completes the right-handed system, directed approximately duskward. The origin of the system is offset north from the planetary center by ~0.2 R_M in accordance with the measured offset of Mercury's dipole field [*Alexeev et al.*, 2008, 2010; *Anderson et al.*, 2008, 2010, 2011; *Johnson et al.*, 2012]. The data have also been aberrated to account for Mercury's orbital motion (using the daily average orbital velocity and an assumed solar wind velocity of 400 km s^{-1}). The use of aberrated data is indicated with prime notation (e.g., X'_{MSM}).

MESSENGER's orbit was eccentric and highly inclined, resulting in almost vertical cuts through the magnetotail plasma sheet several times a day during "hot" and "warm" season orbits. Magnetic field data from an example passage of MESSENGER through the plasma sheet is shown in Figure 1a. MESSENGER began the interval within the southern plasma sheet boundary layer. At approximately 16:17:30 UT the spacecraft passed into the plasma sheet itself, recording diamagnetic depressions of the field indicating the presence of significant plasma. While within the plasma sheet, the sign of $B_{X'}$ reversed several times as the spacecraft encountered the cross-tail current layer. MESSENGER exited the plasma sheet at around 16:26:00 UT, and entered the northern plasma sheet boundary layer.

This manuscript uses data collected during a total of 319 plasma sheet encounters, spanning the entirety of the MESSENGER mission. The plasma sheet crossings are those identified and examined by *Poh et al.* [2017]; for more information regarding their selection criteria, the interested reader is directed to their study.

The selection of crossings are evenly distributed across the midnight meridian and cover a range of downtail distances from ~1 to 3 R_M. Limiting the data to intervals confirmed to lie within the plasma sheet reduces the chance of false positive detections from various phenomena including waves, localized compression regions, and dynamic events on the magnetopause.

2.2. Flux Rope Signatures

The plasma sheet passage displayed in Figure 1a included three flux ropes, and Figure 1b shows a zoom in of the magnetic field for one of these flux ropes; deemed to be an approximately cylindrical, linearly force-free structure. The key features of Figure 1b are the bipolar deflection in B_Z and the local peaks in $B_{Y'}$ and $|B|$. The spacecraft can be approximated as stationary, as the flux rope moves with a much larger relative velocity ($< v > \sim$ 465 km s^{-1}) [*Di Braccio et al.*, 2015]. Previous work has determined that within the magnetotail the prevailing conditions result in the generation of flux ropes in the $\hat{X}_{MSM}$-$\hat{Y}_{MSM}$ plane, with their core fields approximately in the $\pm\hat{Y}_{MSM}$ direction, that travel either planetward or tailward (in the $\pm\hat{X}_{MSM}$ direction)

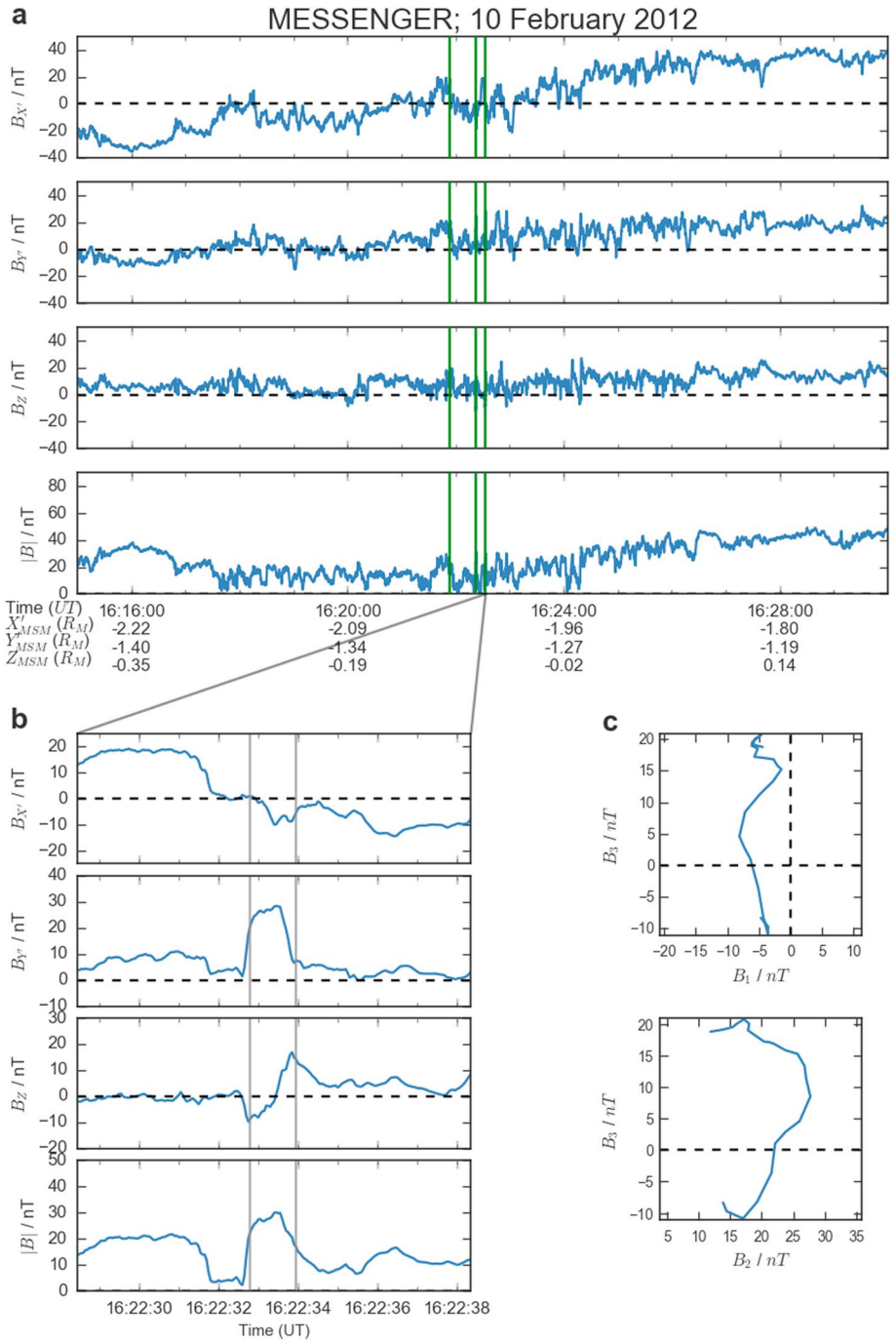

Figure 1. (a) An illustrative plasma sheet crossing, (b) with a zoom in of a flux rope detection, and (c) example MVA hodograms. Figure 1a shows 15 min of 20 Hz MESSENGER magnetometer data in aberrated MSM coordinates; flux rope encounters are shaded green. Figure 1b shows 10 s of data around an in situ flux rope encounter. Once more, the data are presented in aberrated MSM coordinates. The vertical gray bars indicate the region selected for minimum variance analysis (MVA), the resulting magnetic field hodograms (in the MVA system) are shown in Figure 1c.

[*Slavin et al.*, 2003; *Di Braccio et al.*, 2015; *Sun et al.*, 2016]. This configuration gives rise to a bipolar deflection in the north-south component of the field (B_Z), with peaks in the axial direction ($\sim |B_{Y'}|$) and the total field ($|B|$). This signature is highly dependent on the trajectory through the structure, for example, the distance of the spacecraft from the center of the flux rope at the point of closest approach will determine the magnitude of the core field recorded. The signature measured in $B_{X'}$ varies depending on whether the spacecraft

encounters both the upper and lower hemispheres of the flux rope; local peaks or bipolar signatures are not uncommon. More detail and figures depicting the result of various relative trajectories can be found in *Borg et al.* [2012] and *Di Braccio et al.* [2015].

Minimum variance analysis (MVA) was first applied to spacecraft magnetic field observations for the purpose of identifying the normal to magnetic discontinuities: such as current layers [*Sonnerup and Cahill*, 1967]. The method generates three eigenvalues and eigenvectors; the eigenvectors describe a new coordinate system corresponding to the directions of minimum, intermediate, and maximum variance. The degeneracy of the new system can be estimated by comparing the relative sizes of the eigenvalues. A well-defined, distinct three-dimensional system will be described by eigenvalues that are all significantly different from one another [*Khrabrov and Sonnerup*, 1998; *Sonnerup and Scheible*, 1998].

If the spacecraft passes sufficiently close to the axis of a force-free flux rope, then MVA can be used to estimate its orientation and structure [*Sibeck et al.*, 1984; *Elphic et al.*, 1986; *Slavin et al.*, 1989; *Moldwin and Hughes*, 1991; *Xiao et al.*, 2004]. When applied to an encounter with a force-free, cylindrically symmetric flux rope, MVA would be expected to show a clear bipolar signature in the maximum variance direction ($\hat{\mathbf{e}}_3$), a peak in the intermediate direction ($\hat{\mathbf{e}}_2$), and very little variation in the direction of minimum variance ($\hat{\mathbf{e}}_1$). In fact, if the spacecraft passes directly through the center of the flux rope, then the field in the direction of minimum variance will be equal to zero. The combination of the core field peak and the bipolar signature result in a clear rotation of the field in the hodogram of the maximum and intermediate variance directions. This signature is shown in Figure 1c.

2.3. Flux Rope Field Model

A force-free flux rope model is used in this study to estimate some of the physical parameters of the flux rope (e.g., radius and core field) and confirm that the recorded signature is due to the spacecraft's passage through a flux rope. The force-free model represents a simple, stable configuration where plasma pressure gradients are assumed to be negligible ($\nabla \mathbf{P} = 0$) and the flow of plasma is almost entirely parallel to the magnetic field, **B**. In this regime the flux rope is self-balancing, with the magnetic tension force acting inward equal to the magnetic pressure of the strong axial field directed outward. If the flux rope is assumed to be cylindrically symmetric, then the magnetic field of such a structure can be described in cylindrical coordinates by the following equations [*Lundquist*, 1950; *Lepping et al.*, 1990]:

$$B_{\text{axial}} = B_0 J_0(\alpha r') \tag{1}$$

$$B_{\text{azimuthal}} = B_0 H J_1(\alpha r') \tag{2}$$

$$B_r = 0 \tag{3}$$

where B_0 is the magnitude of the magnetic field at the core of the flux rope, $J_0(\alpha r')$ and $J_1(\alpha r')$ are the zeroth and first-order Bessel functions, and $H = \pm 1$, representing the helicity of the flux rope. The Bessel functions depend on the scaled distance from the center of the flux rope ($\alpha r'$). For this work we normalize the results such that the field is purely azimuthal at the edge of the flux rope and completely axial at the center. This corresponds to setting $\alpha = 2.4048$ [*Burlaga*, 1988] and $r' = {}^{r}/_{R_0}$, the impact parameter ($0 \leq r' \leq 1$).

The cylindrically symmetric, constant α (linearly) force-free flux rope model represents the lowest-energy configuration of helical fields [*Priest*, 1990] and so probably better represents flux ropes observed some time after formation.

3. Method

For a full, comprehensive description of the flux rope identification method the reader is directed to *Smith et al.* [2017]. In summary, the following steps are used to identify flux rope encounters:

1. Baseline crossing and peak detection: Significant deflections of the north-south component of the magnetic field are located.
   a. Field deflections where $\Delta B_Z \geq 1\sigma$ are selected (that pass through $B_Z = 0$).
   b. The deflections are required to be coincident with a peak in $|B_Y|$ or $|B|$ (which are identified using a continuous wavelet transform).

2. Minimum variance analysis (MVA): A consistent three-dimensional magnetic structure is confirmed.
    a. The eigenvalue ratios λ_3/λ_2 and λ_2/λ_1 are required to be ≥5.
    b. A small variation in eigenvalue ratios (≤1.75) is needed when the limits of the analysis are varied.
    c. The eccentricity of the maximum-intermediate hodogram must be small ($e \leq 0.9$).
3. Force-free model fitting: The structure is confirmed and physical parameters are estimated.
    a. A good fit to the force-free model is required (modified $\chi^2 \leq 0.15$).
    b. The best fit model impact parameter must be small: $r' \leq 0.5$.

The numerical thresholds were determined empirically by application of the method to trial intervals (both at Mercury and at Earth). Two small changes have been made to the method described by *Smith et al.* [2017]. First, a criterion that the deflection crosses through $B_Z = 0$ has been added. Physically, this corresponds to a requirement that the spacecraft must pass through both the leading and trailing hemispheres of the flux rope. Second, the maximum time window considered has been expanded from 2.5 s to 3 s.

For some of the following analysis the identifications that satisfy the criteria in points one and two will be used, and these will be referred to as MVA-confirmed flux ropes. The motivation for this is to use, when possible, a larger catalog for greater statistical validity. The flux ropes that are judged to be cylindrically symmetric and linearly force-free, those that also satisfy the criteria in point three, form a subset of this larger catalog and will be referred to as the force-free subset.

4. Statistical Results

A total of 248 MVA-confirmed flux ropes were located within the 319 plasma sheet crossings, 74 of which (~30%) satisfactorily fit the force-free model. This force-free fraction is consistent with that determined by *Di Braccio et al.* [2015] ($^{16}/_{49}$ or 33%). It is likely that this fraction is an overestimate; if the flux ropes deviate far from cylindrical and force-free, then they are unlikely to be selected based on the results of their MVA properties (and so the total population of flux ropes will be larger than 248).

4.1. Location and Frequency

The flux rope detections will now be discussed with respect to their rate and magnetospheric location. To that end, Figure 2 includes panels displaying (a) the distribution of MVA-confirmed flux rope detections, (b) the distribution of orbital time within the plasma sheet (termed observation time), and (c) the corresponding rate of flux ropes observed per minute. Figures 2d and 2e then show the rate projected onto the X'_{MSM} and Y'_{MSM} axes, respectively. The color bars for Figures 2d and 2e show the plasma sheet observation time binned along the X'_{MSM} and Y'_{MSM} axes, providing an estimate for how well the rates are defined for each bin.

Figure 2 shows the distributions for all MVA-confirmed flux ropes, but the equivalent plot for force-free flux ropes shows similar results. Figure 2a shows a slight dawn-dusk asymmetry, with 58% of the detections being located on the dawnside of the tail. This is also found to be the case for those detections confirmed to be force-free; 62% are located on the dawnside of the midnight meridian (not shown).

The 319 plasma sheet crossings can be seen to give coverage over most of the magnetotail (Figure 2b). The majority of the coverage can be seen to lie between 1.5 and 2.5 R_M down the tail, and between $-1.5\ R_M \leq Y'_{\mathrm{MSM}} \leq 1.5\ R_M$ azimuthally. There is not a significant dawn-dusk asymmetry in the coverage (the plasma sheet observation time follows a 52%–48% dawn-dusk split), ruling this out as a cause of the imbalance in the numbers observed in Figure 2a.

Normalizing the number of flux ropes observed by the time spent within the plasma sheet reveals that although the largest numbers of flux ropes were observed close to the center of the tail, these also coincide with the locations most often covered by MESSENGER. Figure 2d shows that the rate of flux ropes increases as you move down the tail up until $\sim -2.5\ R_M$. At this point the data coverage is not as comprehensive and so the drop at this point could be due to the relatively small statistics beyond $-2.5\ R_M$ (blue-colored bars indicate relatively low observation time). Figure 2e shows the rate across the magnetotail. The distribution is fairly symmetric within the central magnetotail ($Y'_{\mathrm{MSM}} \leq \pm 0.5\ R_M$), this corresponds approximately to the region surveyed by *Di Braccio et al.* [2015], where no asymmetries were observed. Outside of the central region it can be seen that flux ropes are more commonly observed at dawn; for the bins covering the 0.5 R_M centered on $\sim Y'_{\mathrm{MSM}} = \pm 1$ the rate is 3 times higher at dawn. This result correlates with recent observations of flux ropes [*Sun et al.*, 2016], statistical field distributions [*Poh et al.*, 2017], and the origin of precipitating energetic electrons [*Lindsay et al.*, 2016], though is perhaps not as dramatic. A dawn-dusk asymmetry has also been observed

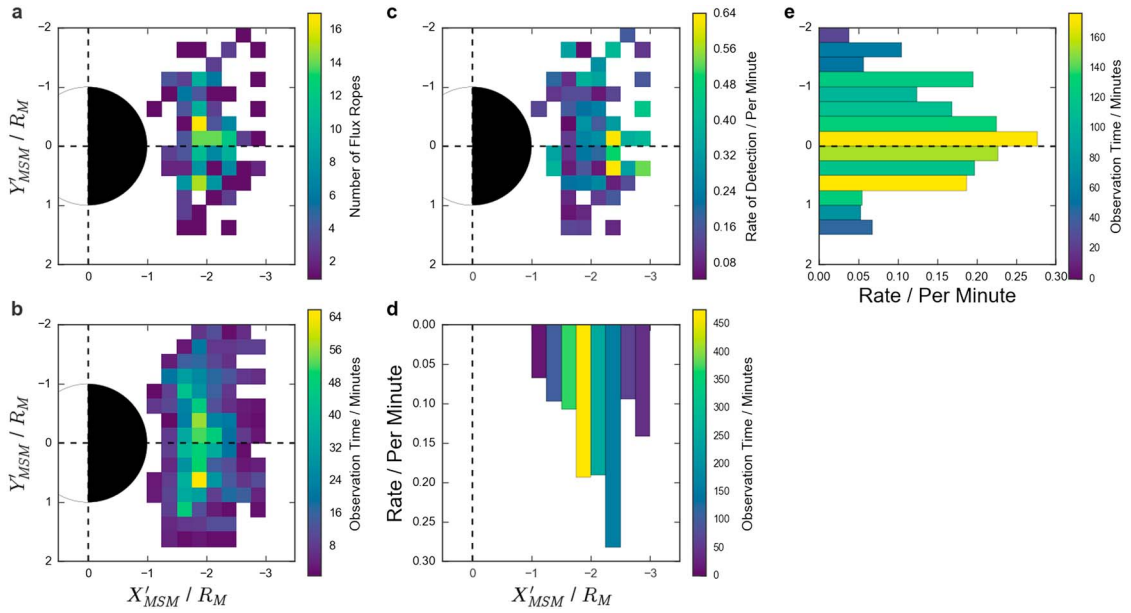

Figure 2. Histograms showing the distribution of 248 (MVA-confirmed) flux ropes within the Hermean magnetotail. Data are binned in $0.25R_M$ increments and projected onto the equatorial plane of the MSM coordinate system. (a) The distribution of flux rope observations. (b) The distribution of plasma sheet observations in minutes per spatial bin. (c) The resulting rate of flux rope observations ($^{\#}/_{T}$). (d, e) The rate projected onto the X'_{MSM} and Y'_{MSM} axes, respectively. The color bars for Figures 2d and 2e show the plasma sheet observation time projected onto the X'_{MSM} and Y'_{MSM} axes; this is shown to provide an approximate measure of how well determined (or how much data) has produced the rates for that region.

for dipolarization fronts [*Sun et al.*, 2016]. This correspondence could be explained by the simulations of *Lu et al.* [2015], who suggest that planetward moving flux ropes may form dipolarization fronts as they rereconnect with the planetary dipole field. Therefore, any asymmetry would be present in both types of event.

The variation in the rate of flux rope observations across the magnetotail (along the X'_{MSM} axis) suggests that the azimuthal extent of flux ropes within Mercury's magnetotail is limited. *Kiehas et al.* [2013] inferred this to be true for terrestrial flux ropes using multiple spacecraft; the absence of contemporaneous flux rope observations at an adjacent spacecraft suggests a limited azimuthal extent. An alternative explanation could be that flux ropes are not well modeled as cylindrical tubes; that they are distorted for much of their length and as such not as easily identifiable.

The peak rate observed in Figures 2d and 2e is around 0.25 flux ropes per minute, just over 3 times the rate observed by *Sun et al.* [2016]. It is possible that by selecting those flux ropes for which $\Delta B_Z \geq 1\sigma$ (as opposed to a fixed limit of $\Delta B_Z \geq 15$ nT [*Sun et al.*, 2016]), we are observing an additional population of small flux ropes. Indeed, if we apply the same selection criterion ($\Delta B_Z \geq 15$ nT) the number of flux ropes in the catalog drops from 248 to 120, and the rate reduces to around 0.1 flux ropes per minute, consistent with their result [*Sun et al.*, 2016].

A dawn-dusk asymmetry in the rate of reconnection products has been observed at Earth [*Walsh et al.*, 2014]; however, the asymmetry is in the opposite direction from that observed by both this and previous studies at Mercury: at Earth, flux ropes are more commonly observed premidnight [*Slavin et al.*, 2005; *Imber et al.*, 2011]. The peak rate of flux ropes observed at Earth was found to be $\sim 1.2 \times 10^{-3}$ min^{-1} [*Imber et al.*, 2011], approximately 200 times smaller than that observed by this work.

The peak rate calculated above (0.25 min^{-1}) is averaged over the plasma sheet observation time and binned along the X'_{MSM} or Y'_{MSM} axis. However, measuring the recurrence in this manner does not fully convey the intermittent nature of the flux rope observations. For example, in Figure 1a, three flux ropes are observed during a single-plasma sheet crossing. The time from the first to the last flux rope is ~39 s, so in this interval the rate of flux rope observation is approximately 5 min^{-1}, much higher than the average (0.25 min^{-1}) would have suggested.

Overall, during 61% of the plasma sheet encounters investigated, no (MVA-confirmed) flux ropes are observed; this fraction increases to 83% when only force-free flux ropes are considered. Figure 3a shows these

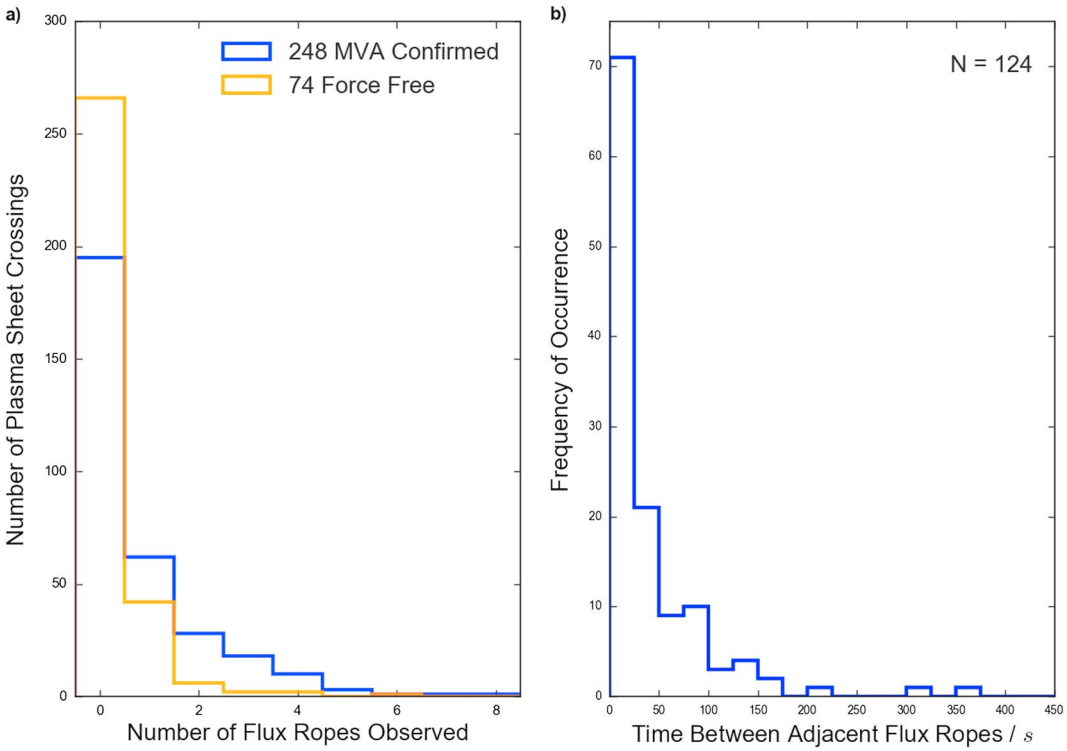

Figure 3. (a) A histogram of the number of MVA-confirmed (blue) and force-free (orange) flux ropes observed during each plasma sheet crossing. (b) The distribution of times between adjacent MVA-confirmed flux ropes.

proportions and also that up to eight flux ropes have been observed in a single crossing. The large fraction of intervals where no flux ropes are observed suggest that reconnection in Mercury's magnetotail is sporadic and occurs in bursts, producing several flux ropes (very rapidly) during each episode before the tail enters a period of relative quiescence. Only 25% of MVA-confirmed flux ropes occur in isolation. This fraction is likely to be an upper limit as some flux ropes are likely not identified.

Figure 3b shows the distribution of times between adjacent MVA-confirmed flux ropes. In total, 124 intervals between adjacent flux ropes are plotted, the vast majority of which are shorter than ~100 s. This suggests that they are likely related to the same reconnection event within the magnetotail. A similarly short interval between adjacent flux ropes has been observed at Earth [*Imber et al.*, 2011].

4.2. Orientation

MVA can be applied to the force-free subset of flux ropes to estimate their approximate orientation [*Sibeck et al.*, 1984; *Elphic et al.*, 1986; *Slavin et al.*, 1989; *Moldwin and Hughes*, 1991; *Xiao et al.*, 2004]. When applied to a force-free flux rope the minimum variance direction ($\hat{\mathbf{e}}_1$) corresponds to the spacecraft passage through the flux rope, the intermediate vector corresponds to the axial direction ($\hat{\mathbf{e}}_2$), and the maximum variance vector completes the right-handed set ($\hat{\mathbf{e}}_3$). Figure 4 shows these MVA results for the force-free subset of flux ropes. The rows show the results for the minimum, intermediate, and maximum variance directions, respectively. Meanwhile, the columns, from left to right, show the X'_{MSM} - Y'_{MSM} projection, the X'_{MSM}-Z_{MSM} projection and the angular difference between the vectors and an MSM base vector of interest.

For Figures 4a(i), 4a(ii), and 4a(iii), the minimum variance direction ($\hat{\mathbf{e}}_1$), the vectors largely lie in the X'_{MSM} to Y'_{MSM} plane. Physically, this suggests that the motion of the flux ropes is limited to this plane, as has been observed by previous studies [*Slavin et al.*, 2003; *Di Braccio et al.*, 2015]. However, the average angular difference between the minimum variance direction and the $\pm\hat{X}'_{MSM}$ axis, is relatively large at 47.5°, the distribution of which in shown in Figure 4a(iii).

Figures 4b(i), 4b(ii), and 4b(iii), showing the results for the intermediate variance direction (($\hat{\mathbf{e}}_2$), representing the approximate direction of the core field show a similar result. The relative magnitude of the vectors is small in panel (b)(ii) compared to that in Figure 4b(i). Figure 4b(iii) shows the distribution of angular differences

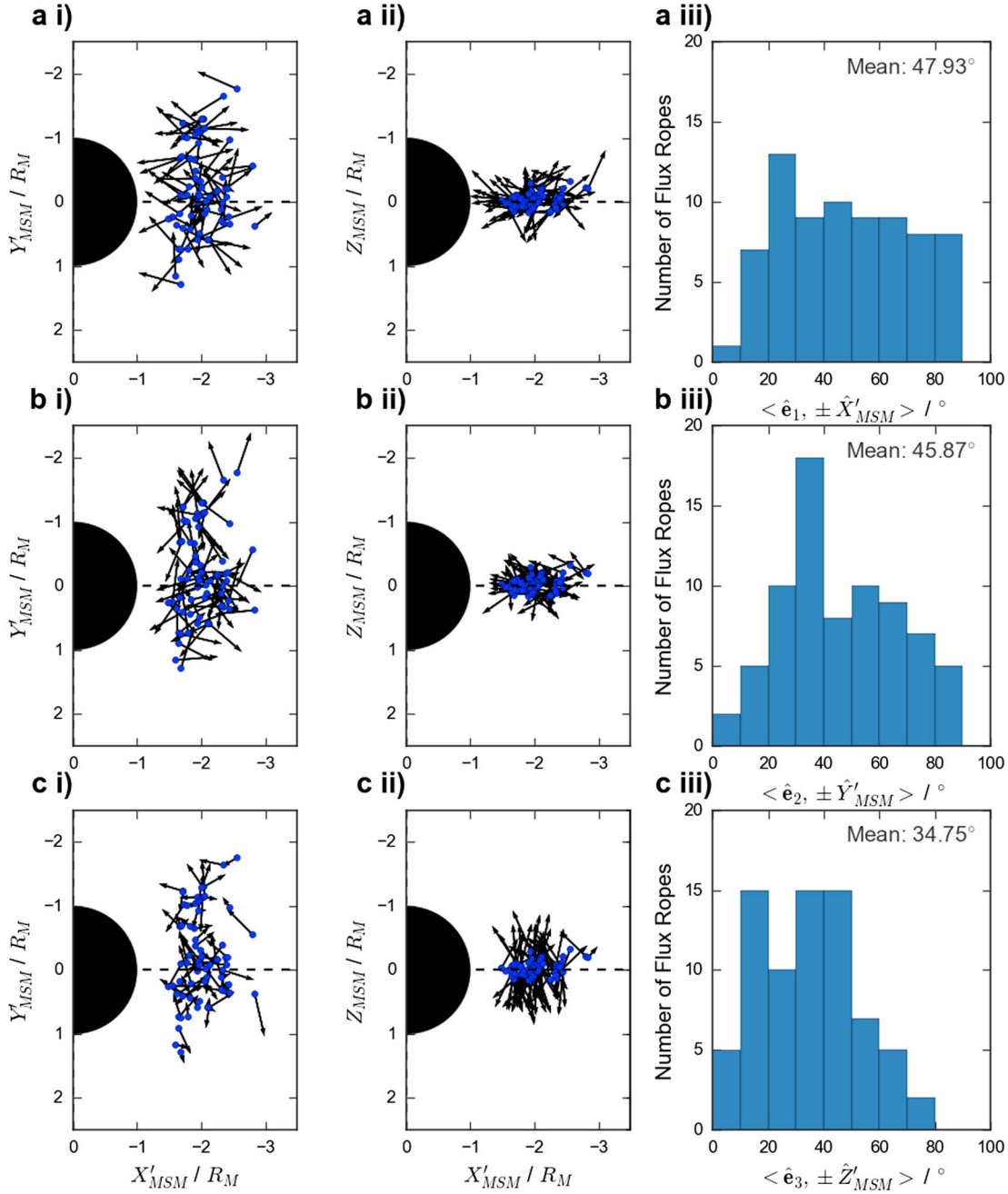

Figure 4. Minimum variance analysis (MVA) results for the 74 force-free flux ropes. Shown are the (left column) X'_{MSM} to Y'_{MSM} and (middle column) X'_{MSM} to Y'_{MSM} projections, respectively. (right column) The angular difference in degrees between the variance vectors and the relevant *MSM* base vector. The rows, from top to bottom, show the minimum, intermediate, and maximum variance vectors.

between the intermediate variance direction and the $\pm\hat{Y}'_{MSM}$ axis. Once more, this shows a relatively large average angular difference (46.5°), suggesting that a large range of flux rope orientations or skews is possible.

Previous studies have commonly observed flux ropes whose axes are tilted in the plane of the magnetic equator at both Earth [*Hughes and Sibeck*, 1987; *Moldwin and Hughes*, 1992; *Slavin et al.*, 2003; *Kiehas et al.*, 2012] and Mercury [*Sun et al.*, 2016]. *Kiehas et al.* [2012] proposed two potential mechanisms to explain this: (a) spreading of the reconnection site east-west from near midnight resulting in a boomerang-shaped flux rope and (b) an asynchronous release of the ends of the flux rope, leading to a self-consistent tilt. Both formation scenarios (a) and (b) would result in the core field deviating from the $\pm Y'_{MSM}$ direction. Scenario (a) may result in a core field directed closer to the azimuthal unit vector, $\hat{\phi}$ (e.g., along lines of constant radial distance

from the planet). The average angular difference between the intermediate variance direction and the azimuthal unit vector was found to be 46.0°; slightly smaller than that found for the $\pm\hat{Y}'_{MSM}$ comparison, but not decisively different. Thus, the results are not sufficient to distinguish between the formation scenarios on a statistical basis; indeed, a combination of both processes is possible [*Kiehas et al.*, 2012].

The final row (Figures 4c(i), 4c(ii), and 4c(iii)) shows that the maximum variance direction is most often aligned with the $\pm\hat{Z}_{MSM}$ direction. However, the angular difference between the vectors still has a relatively large mean value (34.8°).

The results are broadly consistent with the most recent flux rope survey [*Sun et al.*, 2016], though the mean angular differences reported here are slightly larger. This could be due to a larger data set and slightly different selection criteria. Here, for example, we place no firm limit on the size of the B_Z deflection and therefore include smaller-scale events that could perhaps have more extreme tilts (as they would be more susceptible to local perturbations).

There are several selection effects deserving of mention. First, the preliminary signature sought to identify potential flux ropes (section 3, item 1) is a bipolar deflection of B_Z. If the flux ropes do not possess $\Delta B_Z \geq 1\sigma$, then they will not be located by this first step and will therefore not be present in the analysis. It is possible that there are flux ropes excluded from this analysis whose principle axis of variation is poorly aligned with $\pm\hat{Z}_{MSM}$. Second, the identification process described in section 3, item 2 requires the presence of a peak in $\pm B_Y$ or $|B|$, B_X is not considered and it is possible that some highly skewed flux ropes may not be selected (if the peak in $|B|$ is not correctly identified).

An important consideration when applying this analysis is the accuracy of the MVA technique. When MVA is applied to a model force-free flux rope, an impact parameter of $0.5R_0$ results in an angular difference of ~20° between the intermediate variance direction and the true axial direction [*Xiao et al.*, 2004]. A real force-free flux rope (even where the linear and cylindrical symmetry approximations are well founded) will almost certainly result in a larger discrepancy between the intermediate variance axis and the axial direction. In light of this, the relatively large spreads of angular differences observed in Figure 4 are perhaps not unexpected.

4.3. Physical Properties

Figure 5 shows several histograms detailing the distribution of flux rope parameters observed for the force-free subset. Figures 5a and 5b show the duration and size of the magnetic field deflections, respectively, measured from peak to peak of the bipolar B_Z signature. Figure 5c shows the distribution of impact parameters inferred from the force-free model fit. Figures 5d–5f show the distributions of the inferred radius (R_0), core field (B_0), and flux context (Φ_{FR}). The first two panels are plotted for the entire MVA-confirmed catalog, while the latter four only include those confirmed to be force-free.

It is worth noting that there is both a lower and upper cutoff to the duration measured in Figure 5a. The techniques used to identify the events require at least four data points, and thus the lower limit to detection is 0.2 s. In a similar manner, the maximum event length is 3 s; set by the maximum duration explored for the deflection of B_Z. The average duration of 0.83 s for MVA-confirmed flux ropes is slightly larger than that obtained by *Di Braccio et al.* [2015] (0.74 s). The small difference could be explained by the cutoff to the duration applied by this work: no such lower limit was applied by *Di Braccio et al.* [2015]. The mean duration of force-free flux ropes (1.08 s) is found to be greater than that of the larger catalog of MVA-confirmed flux ropes; suggesting that smaller duration flux ropes met the force-free criterion less often. Physically, smaller flux ropes could be more likely to either correspond to those observed soon after their formation (as discussed in section 2.3).

The distribution of Figure 5b increases fairly sharply down to $|\Delta B_Z| \sim 10$ nT. The drop in the distribution below this point could be a result of the requirement that the deflection is greater than the background fluctuations of the field ($|\Delta B_Z| \geq 1\sigma$). It is likely that a population of flux ropes whose magnetic deflections are smaller than 1σ exist, but are not included in this survey. This population may also be missed as a result of the minimum duration of 0.2 s (discussed above).

The distribution of flux rope impact parameters inferred from the force-free fit (Figure 5c) may indicate that the method has resulted in a slight preference for selecting those flux ropes observed at the smallest impact parameters (e.g., $r/R_0 \leq 0.1$). This could be explained by the requirements placed upon the MVA signature: as the spacecraft passage moves farther from the central axis (the impact parameter increases) the MVA results would be expected to be less reliable [*Xiao et al.*, 2004] (and lead to the signature being rejected). Otherwise,

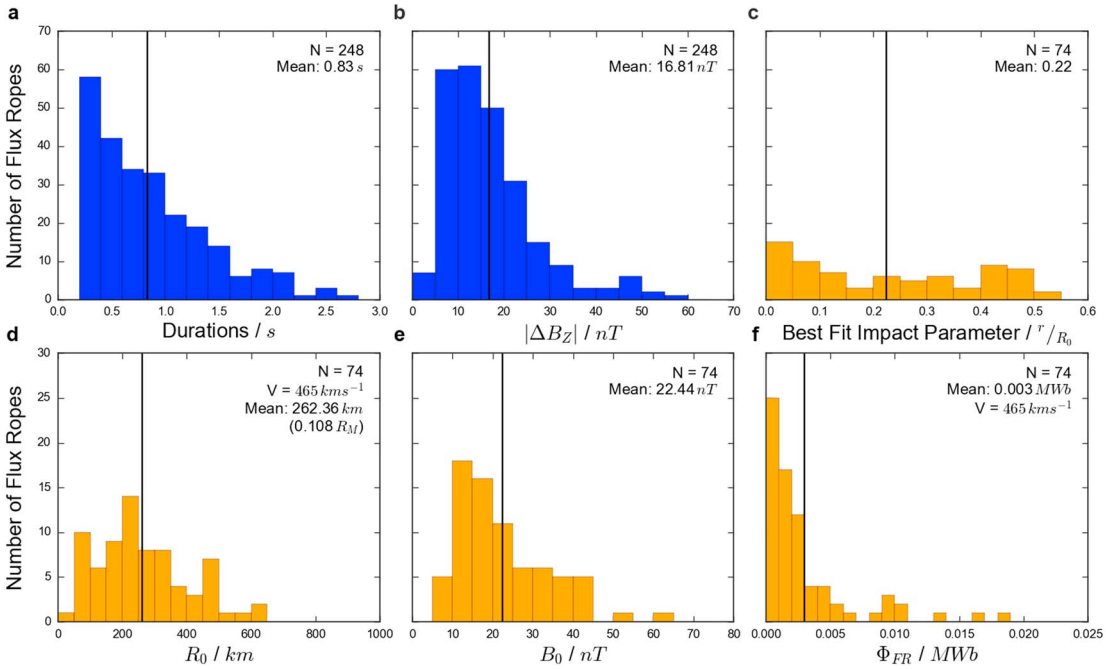

Figure 5. Histograms showing the distribution of several key flux rope parameters. (a, b) Shown for the MVA-confirmed flux ropes (in blue); (c–f) shown only for the force-free subset (in orange) as they require parameters from the successful model fit. The means of the distribution are indicated with black vertical bars (and numerically in the upper right of the panels). Figure 5a shows the duration of the flux ropes as measured by the in situ spacecraft data, between the extremes of the bipolar B_Z variation. Figure 5b shows the distribution of $|\Delta B_Z|$. Figure 5c shows the distribution of best fit impact parameters from the force-free model fit, Figure 5d shows the inferred radius of the flux ropes, calculated assuming a velocity of 465 km s^{-1} and correcting for the impact parameter of the encounter. Figure 5e displays the core fields observed, again inferred from the force-free fit. Figure 5f shows the distribution of flux contained with the flux ropes, calculated using equation (4).

the distribution looks fairly constant, as may be expected: the flux ropes would be contained within the plasma sheet, the entirety of which is traversed by the spacecraft.

Figure 5d) shows the distribution of best fit flux rope radii, calculated using the observed duration, best fit model impact parameter, and an assumed average speed of 465 km s^{-1} [*Di Braccio et al.*, 2015]. The use of an average, and not a local speed, is not ideal. *Di Braccio et al.* [2015] measured the Alfvén speed (V_A) of the adjacent plasma sheet and found values to range from as low as ~100 km s^{-1} to over 1000 km s^{-1}. In addition to this order of magnitude variation in the local plasma sheet, it is likely that within the (plasma depleted) reconnection flow the Alfvén speed is higher. For these reasons the radii calculated should be regarded as lower limits. The mean R_0 inferred from the catalog is 262 km (0.11 R_M), consistent with previous work [*Slavin et al.*, 2012; *Di Braccio et al.*, 2015], though slightly smaller; perhaps for the reasons outlined above. A typical plasma sheet density of between 1 and 10 cm^{-3} [*Gershman et al.*, 2014] suggests that the ion inertial length in Mercury's magnetotail plasma sheet is ~78–228 km; only slightly smaller than the radius of the observed flux ropes. Therefore, these flux ropes are of similar nature to the ion-scale flux ropes recently identified at the Earth's magnetopause [*Eastwood et al.*, 2016].

The distribution of core field inferred from the force-free fitting (B_0) is provided in Figure 5e). The mean B_0 observed is found to be 22.44 nT, smaller than that observed by *Di Braccio et al.* [2015] (41 nT) and more comparable to that observed at the Earth (20 nT) [*Slavin et al.*, 2003].

The flux contained within the flux rope can be obtained from the results of the force-free fit:

$$\Phi_{FR} = \frac{1}{\alpha} 2\pi B_0 R_0^2 J_1(\alpha) \tag{4}$$

where Φ_{FR} is the flux content of the flux rope, α is a constant from the force-free fit (taken to be 2.4048 [*Burlaga*, 1988]), B_0 is the strength of the core field, R_0 is the radius of the flux rope, and $J_1(\alpha)$ is the first-order Bessel function. As this equation requires the radius of the flux rope, it is implicitly dependent on the flux rope velocity (once more assumed to be 465 km s^{-1} [*Di Braccio et al.*, 2015]). The distribution of flux content is displayed in Figure 5f. The average Φ_{FR} is found to be 0.003 MWb, consistent with the previous estimate

of *Di Braccio et al.* [2015]. In comparison, the average flux content of FTEs at Mercury's magnetopause has been found to be 0.06 MWb [*Imber et al.*, 2011], suggesting that the flux contained within magnetotail flux ropes is negligible when considering the closure of magnetic flux from the magnetosphere. Therefore, the majority of the flux closure at Mercury must occur during continued lobe reconnection at the x-lines that generate flux ropes [*Richardson et al.*, 1987; *Di Braccio et al.*, 2015].

5. Discussion

The survey results will now be discussed with respect to spatial variations across the magnetotail and factors affecting flux rope creation.

5.1. Reconnection Location

Although no direct encounters with the NMNL (near-Mercury neutral line) are reported by this study, its relative location can be inferred from the direction of motion of the observed flux ropes. In total, 55% of the observed flux ropes are moving toward the planet, these flux ropes are observed between 1.25 and 3 R_M down the Hermean tail. On this basis it could be inferred that the NMNL often lies downtail, beyond MESSENGER's orbit ($R \leq 3\ R_M$). This broad result agrees with the preliminary analysis in section 4.1 and the recent statistical study of *Poh et al.* [2017], who inferred that the average location of the NMNL was at $X'_{\mathrm{MSM}} \sim -3R_M$.

Figure 6 shows how the distributions of tailward and planetward moving flux ropes compare. Figures 6a and 6b show the distribution of the rates of flux ropes observed in each sector. Qualitatively, they show similar distributions around the midnight ($X'_{\mathrm{MSM}} = 0$); however, it can be seen that the more distant (downtail) detections postmidnight are almost solely due to planetward moving flux ropes (e.g., $X'_{\mathrm{MSM}} \leq -2$). Figure 6c shows the difference between Figures 6a and 6b. The majority of sectors are negative (red) indicating that planetward moving flux ropes are more common, especially postmidnight. Again, this perhaps suggests that the location of the NMNL (on average) lies downtail, beyond the coverage of MESSENGER.

Figure 6d shows the rate of tailward and planetward moving (MVA-confirmed) flux ropes projected along the X'_{MSM} axis. The distributions are similar for both populations, indicating that the location of the NMNL is likely extremely variable and can, perhaps under strong driving/loading conditions [*Slavin et al.*, 2010], be located very close to the planet. *Di Braccio et al.* [2015] inferred the location of the NMNL to be within ~2 and 3 R_M of the planet, a result consistent with a highly mobile x-line within the coverage of MESSENGER.

Figure 6e shows the distribution of flux ropes across the Hermean magnetotail, along the $\hat{Y}'_{\mathrm{MSM}}$ axis. The slight dawn-dusk asymmetry, highlighted in section 4.1, is shown here to be almost entirely due to a portion of the planetward moving flux rope population (red bars). Of the planetward moving flux ropes, 62% are located dawnward of the midnight meridian, compared to 52% of tailward moving flux ropes. This could be explained by the NMNL forming farther down the magnetotail on the dawn flank. An asymmetric x-line has been observed at Jupiter, though in the opposite respect: the Jovian x-line is located closer to planet postmidnight [*Vogt et al.*, 2010].

While this is a statistical result, it may be expected that on each occasion the NMNL forms at a given location before retreating down the magnetotail, as was observed during the second [*Slavin et al.*, 2009, 2012] and third MESSENGER flybys [*Slavin et al.*, 2010]. In these intervals the motion was diagnosed by observing a transition from tailward moving flux ropes (and/or associated traveling compression regions, TCRs) to planetward moving structures (as at Earth, cf. *Baker et al.* [1996]). In both flybys the transition between tailward and planetward motion occurred on timescales of the order of minutes to tens of minutes, comparable to the average duration of plasma sheet passages in this study (4.6 min). In this statistical work, a transition from tailward to planetward moving (MVA-confirmed) flux ropes was observed 34 times, at locations ranging from $X'_{\mathrm{MSM}} = -1.35$ to $-2.82\ R_M$ (i.e., across the full scope of this study). A total of 62 chains of more than one (MVA-confirmed) flux ropes were observed, and so 55% of flux rope chains show evidence of neutral line retreat, indicating that this is a relatively common occurrence.

5.2. Magnetotail Driving

Reconnection at the dayside magnetopause, if not matched by reconnection in the magnetotail, results in a buildup of open flux in the magnetotail lobes. At Earth this is known as the growth phase of a substorm [*Akasofu*, 1964]. This buildup of magnetic flux can be observed as an increase in the lobe magnetic field strength [*McPherron et al.*, 1973; *Baker et al.*, 1996] or in the magnetotail flaring angle [*Fairfield*, 1985]. It could be expected that reconnection becomes more likely within the magnetotail as the lobe field strength

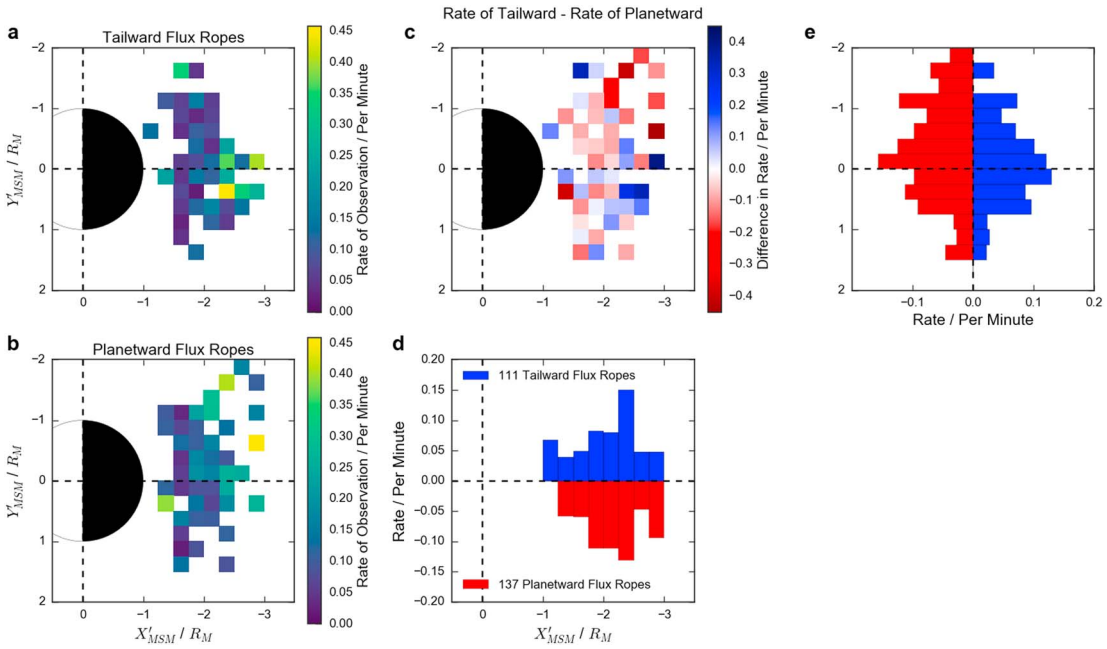

Figure 6. Histograms showing the rate of observation of (a) 111 tailward and (b) 137 planetward moving MVA-confirmed flux ropes. Data are binned in 0.25 R_M increments and projected onto the equatorial plane of the MSM coordinate system. (c) The rate of tailward moving flux ropes minus the rate of the planetward moving flux ropes. Positive (blue) values indicate regions where tailward moving flux ropes are observed more often, while negative (red) regions show locations where planetward moving flux ropes are more commonly observed. Figures 5d and 5e show the rates of planetward (red) and tailward (blue) moving flux ropes binned along the X'_{MSM} and Y'_{MSM} axes, respectively.

increases and the plasma sheet thins, magnetospheric phenomena that have been observed at Mercury [*Sun et al.*, 2015]. Ideally, this would be explored using data from multiple spacecraft, allowing the simultaneous measurement of lobe field strength and in situ flux rope encounters, especially at Mercury where the relative timescales are very short [*Slavin et al.*, 2009, 2012]. However, lacking multipoint observations, the average lobe field ($< |B|_{\text{Lobe}} >$) was recorded shortly before each plasma sheet passage (an average of 4 m 43 s before). A background model lobe field can then be subtracted:

$$|B|^{\text{Model}}_{\text{Lobe}}(|X'_{\text{MSM}}|) = A|X'_{\text{MSM}}|^G + B_0 \tag{5}$$

where the values of the variables A, G, and B_0 were determined to be 86.4, −3.1, and 41.4, respectively, by *Poh et al.* [2017]. The aim of the subtraction is to provide an estimate of whether the lobe field is relatively enhanced or diminished compared to other orbits. Figure 7 shows how the difference in lobe field strength is related to the likelihood of flux ropes being observed during a plasma sheet crossing. The fraction of crossings plotted is the number of crossings during which at least one (MVA-confirmed) flux rope is observed (for a given lobe field strength) divided by the total number of crossings. The color bar is used to show the total number of crossings for the relative lobe field strength. For example, during two separate orbital passes the lobe field strength was over 40 nT greater than the model prediction; during both of the subsequent plasma sheet encounters, at least one flux rope was observed (giving them both fractions of 1). It can be clearly seen from Figure 7 that the larger the lobe field strength, relative to a background level, the more likely MESSENGER was to observe flux ropes during the plasma sheet passage. Though Figure 7 is plotted for the MVA-confirmed flux rope catalog, the same trend is found if the figure is repeated for the force-free subset.

5.3. Magnetotail Shear

Previous work at the Earth found a time-delayed correlation between the B_Y component of the magnetic field in the IMF and the measured B_Y in the core of flux ropes observed in the center of the magnetotail. *Moldwin and Hughes* [1992] recorded the hourly average of the IMF and found that 87% of the 39 flux ropes observed had core fields orientated in the same direction. Later, *Slavin et al.* [2003] reported 79% of the 28 flux rope core fields in their sample agreed with the preceding IMF. More recently, *Borg et al.* [2012] performed a similar study with a sample size of 27, observing only a weak correlation. At Mercury, no contemporaneous upstream measurements of the IMF are possible given the presence of a solitary spacecraft. However, reconnection

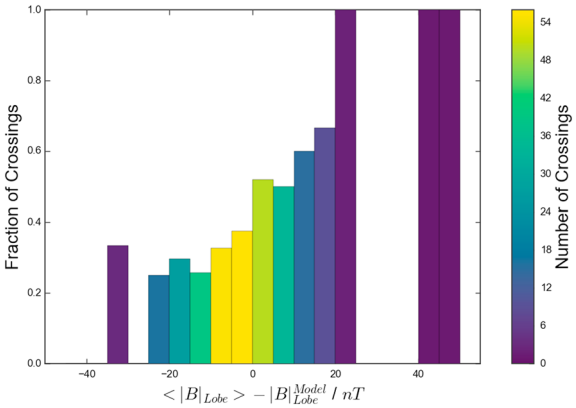

Figure 7. The fraction of crossings during which (MVA-confirmed) flux ropes were observed plotted against the relative lobe field strength measured just prior to the plasma sheet encounter. The model lobe field strength (from equation (5)) [*Poh et al.*, 2017] is subtracted from the average lobe field (measured shortly before entering the plasma sheet boundary layer) to calculate the relative lobe field strength. The color bar indicates the number of crossings present in each bin.

between the IMF and the dayside magnetopause will result in transport of the IMF B_Y into the magnetotail [*Fairfield*, 1979; *Cowley and Hughes*, 1983; *Petrukovich*, 2011], either through direct convection [*Dungey*, 1965] or asymmetric flux transport [*Tenfjord et al.*, 2015]. Estimates of the timescale for the transport of the IMF from the solar wind to the terrestrial neutral sheet vary between ∼1 and 3 h, depending on the solar wind conditions [*Rong et al.*, 2015; *Browett et al.*, 2017]. At Mercury it is likely that this timescale is much shorter, owing to the smaller size of the magnetosphere and stronger solar wind modulation [*Burlaga*, 2001; *Slavin et al.*, 2010]. A full consideration of the timescale involved in the transfer of the IMF to the neutral sheet at Mercury is both beyond the scope of this work and unlikely to be possible with the single-point measurements available. There are two unknown timescales, at Mercury, of importance to this investigation, the first of which is the time for the IMF B_Y to penetrate the magnetotail. The second is the timescale of variation of B_Y, both in the solar wind and the magnetotail.

The B_Y measured in the magnetotail has several major contributing factors: (a) interaction with the IMF, (b) magnetotail flaring, and (c) local fluctuations of the plasma sheet. Source (a) is of primary interest to this study in terms of its effect on the development of the core field of the flux rope [*Moldwin and Hughes*, 1992; *Borg et al.*, 2012]. Source (b), flaring of the magnetotail, is significant in that MESSENGER's orbit lies within the flaring region; *Poh et al.* [2017] estimated that the flaring region statistically ends at $\sim -3.5\ R_M$ (the extrapolated location where lobe field strength asymptotes). Quantifying the third source of magnetotail B_Y is nontrivial given the relative timescales of the spacecraft motion and plasma sheet fluctuations. Instead, their effect is minimized by selecting lobe intervals at a distance from the plasma sheet. The B_Y component due to the skew of the magnetotail (caused by the angle of solar wind incidence) is assumed to be small, having been corrected for with the use of an aberrated coordinate system (e.g., $B_{Y'}$) [*Fairfield*, 1979].

To isolate the $B_{Y'}$ due to the interaction with the IMF we apply a two-dimensional model to allow the subtraction of an empirical model flared field. Figure 8a shows a three-dimensional plot, where the points indicate the location of the measured lobe intervals and their corresponding values of $B_{Y'}$. The surface and color bar show the least squares quadratic model fit expressed in equation (6):

$$B_{Y'}^{\text{Model}} = a\left(X'_{\text{MSM}}\right)^2 + b\left(Y'_{\text{MSM}}\right)^2 + cX'_{\text{MSM}}Y'_{\text{MSM}} + dX'_{\text{MSM}} + eY'_{\text{MSM}} + f \tag{6}$$

A linear (planar) fit was also tested and found to result in larger residuals: it did not accurately describe the reduction in flaring with downtail distance. The values of the coefficients obtained from the least squares fit are shown in Table 1. The model can be seen to asymptote/flatten at $\sim -3.5\ R_M$, this could be interpreted as the end of the flaring region, consistent with the findings of *Poh et al.* [2017]. However, the model asymptotes to a nonzero value of $B_{Y'}$, perhaps due to the relative scarcity of data beyond $\sim -2.5\ R_M$. Though the model will describe the average tail flaring of the magnetotail, it is likely highly variable and dependent on recent solar wind conditions.

Figure 8b) shows the maximum B'_Y measured within the flux rope (as an estimate of the core field strength) plotted against the difference between the lobe field measurement (made prior to the flux rope encounter) and the model value calculated from equation (6). The gray points and error bars show the individual measurements and $\pm 1\sigma$ of the lobe $B_{Y'}$. The blue solid points show the mean and standard error of the mean of the data binned every 5 nT. The blue line indicates the best fit to the data (in gray).

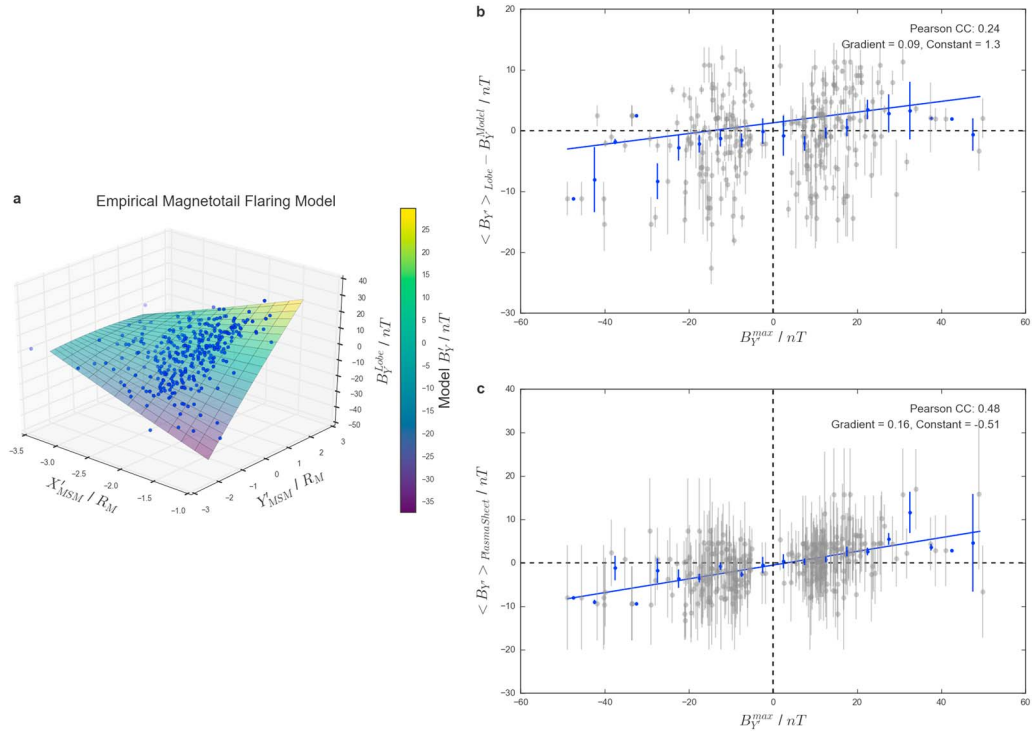

Figure 8. (a) The distribution of B_Y measured across the tail within the lobe (projected onto the $X'_{MSM} - Y'_{MSM}$ plane). The surface shows the least squares quadratic fit to the data, the color bar corresponds to the resulting modeled value of B_Y. (b) The model subtracted value of B_Y measured in the lobe plotted against the maximum B_Y recorded in the 248 MVA-confirmed flux ropes. (c) The average B'_Y measured within the plasma sheet compared to the maximum B_Y recorded within the 248 MVA-confirmed flux ropes. For Figures 8b and 8c the gray points indicate individual flux ropes (with the error bars showing $\pm 1\sigma$) while the data are also placed into 5 nT bins, the mean and standard error of the mean are shown in blue. The blue lines show the result of a least squares fit to the gray points. The values of the Pearson correlation coefficient and least squares fit are provided in the top right of the panels.

The correlation shown by Figure 8b is weak; only 58% of the observed flux ropes have core directions consistent with the preceding lobe field orientations. The first potential explanation is down to the timescales of the penetration of the IMF and variation of B'_Y. The lobe value is measured (on average) ~5–10 min before the flux ropes are observed, so it is perhaps likely that the B'_Y measured is not the same as that present in the current sheet during the formation of the flux rope. Also, the variation in B'_Y is evident in the relative size of the gray error bars. It is also true that the study includes a large number of small-scale flux ropes, whose core orientation and strength is likely to be strongly dependent on the local conditions at their formation; conditions that are not well explored with such broad averaging and unknown timing. Perhaps less critically, the maximum B'_Y measured during the flux rope is a conservative lower limit to the core field of the flux rope; very few encounters will pass directly through the strongest core field at the center of the flux ropes. Similarly, as shown in section 4.2, a large number of the observed flux ropes have a significant tilt to their core orientation (in the X'_{MSM}-Y'_{MSM} plane) meaning that the peak B'_Y value will again underestimate the core field strength. Finally, the value of B'_Y due to the flaring of the tail will vary over time depending on recent solar wind conditions; during periods of strong (weak) driving, the tail flaring angle will increase (decrease), increasing (reducing) the contribution of tail flaring to the observed B'_Y.

Figure 8c shows the relationship between the average B'_Y measured within the central plasma sheet and the maximum B'_Y measured during the flux rope. Of the flux ropes, 67% are oriented in a manner consistent with prevailing plasma sheet B'_Y, though the error bars (standard deviations) are relatively large, indicating that the plasma sheet B'_Y fluctuates significantly. Some inconsistencies would be expected as we are not observing the local plasma sheet where the flux ropes are formed, but the plasma sheet before, during, and after their passage past the spacecraft. It may be expected that the core fields would correlate strongly with the local Hall field [*Teh et al.*, 2014].

Table 1. Least Squares-Derived Coefficients for Equation (6)

Coefficient	*a*	*b*	*c*	*d*	*e*	*f*
Value	0.36	−0.43	7.79	2.86	27.3	1.32

The inverse of the gradient of the linear fit is large, indicating that (statistically) the core fields observed are just over 6 times the average B'_Y measured in the plasma sheet at a similar time. As mentioned above, the $B'^{max}_{Y'}$ plotted here is a lower limit of the core field strength due to the observed flux rope tilt and largely nonzero impact parameters. Though the results are generally consistent with the B'_Y in the nearby plasma sheet, resulting in the generation of the core field, there are a significant number of exceptions similar to the observations of *Borg et al.* [2012] at Earth, perhaps due to variations in the strength of the local guide field [*Teh et al.*, 2014].

6. Conclusion

The MESSENGER mission provides a wealth of crossings through the magnetotail plasma sheet. An automated method has been applied to 319 of these crossings to identify flux ropes. The method initially identifies intervals when the north-south component of the magnetic field passes through zero. These are cross-checked to select those that occur concurrently with peaks (identified using a CWT: continuous wavelet transform) in the dawn-dusk component and/or total magnetic field. Flux ropes are then selected as those possessing well-defined MVA coordinate systems with clear rotations of the field. In total, 248 flux ropes are located, 74 of which are then found to be well represented by a cylindrically symmetric, constant α force-free model.

A small dawn-dusk asymmetry is observed, with 58% of flux ropes observed postmidnight. In situ flux rope encounters are intermittent, with 61% of plasma sheet crossings yielding no flux ropes. However, flux rope observations are found to be more likely if the preceding lobe field is relatively enhanced. Flux ropes are observed at up to a rate of ~5 min^{-1} during active intervals; however, the average peak rate (post midnight) is only 0.25 min^{-1}. Only 25% of flux ropes are observed in isolation; the majority occur in close succession with the time between adjacent flux ropes generally being less than 100 s. The radii of the identified force-free flux ropes are found to be of the order of ion inertial length in Mercury's magnetotail plasma sheet.

Minimum variance analysis suggests that the majority of the motion of the flux ropes is confined to the X'_{MSM}-Y'_{MSM} plane. It is also found that a large fraction of the flux ropes observed display a significant skew in the X'_{MSM}-Y'_{MSM} plane, perhaps due to an asynchronous release of the ends of the flux ropes, or an east-west spread of the reconnection location.

Very little difference is observed between the downtail distributions of planetward and tailward moving flux ropes identifications, suggesting that the x-line is highly mobile over the region surveyed. Across the magnetotail (in the dawn-dusk plane) it is found that the majority of postmidnight identifications are moving planetward, perhaps suggesting that the x-line is located farther down the tail in this region. In addition, 55% of flux rope chains show some evidence of neutral line retreat.

The effect of the IMF on the flux rope core field orientation is indirectly probed using the lobe and plasma sheet fields. Very weak correlations are found with the lobe field, and a slightly stronger relationship is found with the plasma sheet field. The core field of the flux ropes is found to be ~6 times greater than the azimuthal component of the magnetic field in the plasma sheet. The upcoming European Space Agency (ESA) Bepi-Colombo mission to Mercury will be well positioned to shed more light on these topics, with two orbiters allowing multipoint observations.

Acknowledgments
The data used in this study were available from the Planetary Data System (PDS): http://pds.jpl.nasa.gov. A.W.S. is funded by a SEPnet PhD studentship. The contributions by one of the authors (J.A.S.) were supported by NASA's Discovery Data Analysis Program (NNX15K88G), Heliophysics Supporting Research (NNX15AJ68G), and Living With a Star (NNX16AJ67G). C.M.J. is supported by STFC Ernest Rutherford FellowshipST/L004399/1. R.C.F. is supported by STFC Ernest Rutherford FellowshipST/K004298/2. A.W.S. would like to thank S.D. Browett for helpful discussion.

References

Akasofu, S.-I. (1964), The development of the auroral substorm, *Planet. Space Sci.*, *12*(4), 273–282, doi:10.1016/0032-0633(64)90151-5.

Alexeev, I. I., E. S. Belenkaya, S. Y. Bobrovnikov, J. A. Slavin, and M. Sarantos (2008), Paraboloid model of Mercury's magnetosphere, *J. Geophys. Res.*, *113*, A12210, doi:10.1029/2008JA013368.

Alexeev, I. I., E. S. Belenkaya, J. A. Slavin, B. J. Anderson, D. N. Baker, S. A. Boardsen, C. L. Johnson, M. E. Purucker, M. Sarantos, and S. C. Solomon (2010), Mercury's magnetospheric magnetic field after the first two MESSENGER flybys, *Icarus*, *209*(1), 23–39, doi:10.1016/j.icarus.2010.01.024.

Anderson, B., M. Acuña, D. Lohr, J. Scheifele, A. Raval, H. Korth, and J. Slavin (2007), The magnetometer instrument on MESSENGER, *Space Sci. Rev.*, *131*(1-4), 417–450, doi:10.1007/s11214-007-9246-7.

Anderson, B. J., M. H. Acuña, H. Korth, M. E. Purucker, C. L. Johnson, J. A. Slavin, S. C. Solomon, and R. L. McNutt (2008), The structure of Mercury's magnetic field from MESSENGER's first flyby, *Science*, *321*, 5885.

Anderson, B. J., et al. (2010), The magnetic field of Mercury, *Space Sci. Rev.*, *152*(1), 307–339, doi:10.1007/s11214-009-9544-3.
Anderson, B. J., C. L. Johnson, H. Korth, M. E. Purucker, R. M. Winslow, J. A. Slavin, S. C. Solomon, R. L. McNutt, J. M. Raines, and T. H. Zurbuchen (2011), The global magnetic field of Mercury from MESSENGER orbital observations, *Science*, *333*(6051), 1859–1862, doi:10.1126/science.1211001.
Anderson, B. J., C. L. Johnson, H. Korth, R. M. Winslow, J. E. Borovsky, M. E. Purucker, J. A. Slavin, S. C. Solomon, M. T. Zuber, and R. L. McNutt (2012), Low-degree structure in Mercury's planetary magnetic field, *J. Geophys. Res.*, *117*, E00L12, doi:10.1029/2012JE004159.
Baker, D. N., J. A. Simpson, and J. H. Eraker (1986), A model of impulsive acceleration and transport of energetic particles in Mercury's magnetosphere, *J. Geophys. Res.*, *91*(1), 8742–8748, doi:10.1029/JA091iA08p08742.
Baker, D. N., T. I. Pulkkinen, V. Angelopoulos, W. Baumjohann, and R. L. McPherron (1996), Neutral line model of substorms: Past results and present view, *J. Geophys. Res.*, *101*(A6), 12,975–13,010, doi:10.1029/95JA03753.
Borg, A. L., M. Taylor, and J. P. Eastwood (2012), Observations of magnetic flux ropes during magnetic reconnection in the Earth's magnetotail, *Ann. Geophys.*, *30*(5), 761–773.
Browett, S. D., R. C. Fear, A. Grocott, and S. E. Milan (2017), Timescales for the penetration of IMF B_y into the Earth's magnetotail, *J. Geophys. Res. Space Physics*, *122*, 579–593, doi:10.1002/2016JA023198.
Burlaga, L. (2001), Magnetic fields and plasmas in the inner heliosphere: Helios results, *Planet. Space Sci.*, *49*(14), 1619–1627, doi:10.1016/S0032-0633(01)00098-8.
Burlaga, L. F. (1988), Magnetic clouds and force-free fields with constant alpha, *J. Geophys. Res.*, *93*(A7), 7217–7224, doi:10.1029/JA093iA07p07217.
Christon, S. (1987), A comparison of the Mercury and Earth magnetospheres: Electron measurements and substorm time scales, *Icarus*, *71*(3), 448–471, doi:10.1016/0019-1035(87)90040-6.
Cowley, S. W. H. (1981), Magnetospheric asymmetries associated with the *y*-component of the IMF, *Space Sci. Rev.*, *29*, 79–96.
Cowley, S. W. H. (1981), Magnetospheric and ionospheric flow and the interplanetary magnetic field, in *Physical Basis of the Ionosphere in the Solar-Terrestrial System, AGARD CP-295*, pp. 4.1–4.14, Advisory Group for Aerospace Res. and Dev., NATO, Neuilly sur Seine, France.
Cowley, S. W. H., and W. J. Hughes (1983), Observation of an IMF sector effect in the Y magnetic field component at geostationary orbit, *Planet. Space Sci.*, *31*(1), 73–90, doi:10.1016/0032-0633(83)90032-6.
Di Braccio, G. A., et al. (2015), MESSENGER observations of flux ropes in Mercury's magnetotail, *Planet. Space Sci.*, *115*, 77–89, doi:10.1016/j.pss.2014.12.016.
Dungey, J. W. (1961), Interplanetary magnetic field and the auroral zones, *Phys. Rev. Lett.*, *6*, 47–48.
Dungey, J. W. (1965), The length of the magnetospheric tail, *J. Geophys. Res.*, *70*(7), 1753–1753, doi:10.1029/JZ070i007p01753.
Eastwood, J. P., and S. A. Kiehas (2015), *Magnetotails in the Solar System*, pp. 269–287, John Wiley, Hoboken, N. J.
Eastwood, J. P., et al. (2016), Ion-scale secondary flux-ropes generated by magnetopause reconnection as resolved by MMS, *Geophys. Res. Lett.*, *43*, 4716–4724, doi:10.1002/2016GL068747.
Elphic, R. C., C. A. Cattell, K. Takahashi, S. J. Bame, and C. T. Russell (1986), ISEE-1 and 2 observations of magnetic flux ropes in the magnetotail: FTE's in the plasma sheet?, *Geophys. Res. Lett.*, *13*(7), 648–651, doi:10.1029/GL013i007p00648.
Eraker, J. H., and J. A. Simpson (1986), Acceleration of charged particles in Mercury's magnetosphere, *J. Geophys. Res.*, *91*(A9), 9973–9993, doi:10.1029/JA091iA09p09973.
Fairfield, D. H. (1979), On the average configuraton of the geomagnetic tail, *J. Geophys. Res.*, *84*(A5), 1950–1958, doi:10.1029/JA084iA05p01950.
Fairfield, D. H. (1985), Solar wind control of magnetospheric pressure (CDAW 6), *J. Geophys. Res.*, *90*(1), 1201–1204, doi:10.1029/JA090iA02p01201.
Gershman, D. J., J. A. Slavin, J. M. Raines, T. H. Zurbuchen, B. J. Anderson, H. Korth, D. N. Baker, and S. C. Solomon (2014), Ion kinetic properties in Mercury's pre-midnight plasma sheet, *Geophys. Res. Lett.*, *41*, 5740–5747, doi:10.1002/2014GL060468.
Hones, E. W. (1977), Substorm processes in magnetotail: Comments on 'On hot tenuous plasmas, fireballs, and boundary-layers in Earth's magnetotail' by L. A. Frank, K. L. Ackerson, and R. P. Lepping, *J. Geophys. Res.*, *82*(35), 5633–5640.
Hones, E. W., D. N. Baker, S. J. Bame, W. C. Feldman, J. T. Gosling, D. J. McComas, R. D. Zwickl, J. A. Slavin, E. J. Smith, and B. T. Tsurutani (1984), Structure of the magnetotail at 220 R_E and its response to geomagnetic activity, *Geophys. Res. Lett.*, *11*(1), 5–7, doi:10.1029/GL011i001p00005.
Huang, C.-S. (2002), Evidence of periodic (2–3 hour) near-tail magnetic reconnection and plasmoid formation: Geotail observations, *Geophys. Res. Lett.*, *29*(24), 42–44, doi:10.1029/2002GL016162.
Hughes, W. J., and D. G. Sibeck (1987), On the 3-dimensional structure of plasmoids, *Geophys. Res. Lett.*, *14*(6), 636–639, doi:10.1029/GL014i006p00636.
Ieda, A., S. Machida, T. Mukai, Y. Saito, T. Yamamoto, A. Nishida, T. Terasawa, and S. Kokubun (1998), Statistical analysis of the plasmoid evolution with Geotail observations, *J. Geophys. Res.*, *103*(A3), 4453–4465, doi:10.1029/97JA03240.
Imber, S. M., J. A. Slavin, H. U. Auster, and V. Angelopoulos (2011), A THEMIS survey of flux ropes and traveling compression regions: Location of the near-Earth reconnection site during solar minimum, *J. Geophys. Res.*, *116*, A02201, doi:10.1029/2010JA016026.
Johnson, C. L., et al. (2012), MESSENGER observations of Mercury's magnetic field structure, *J. Geophys. Res.*, *117*, E00L14, doi:10.1029/2012JE004217.
Khrabrov, A. V., and B. U. Ö. Sonnerup (1998), Error estimates for minimum variance analysis, *J. Geophys. Res.*, *103*(A4), 6641–6651, doi:10.1029/97JA03731.
Kiehas, S. A., V. Angelopoulos, A. Runov, M. B. Moldwin, and C. Möstl (2012), On the formation of tilted flux ropes in the Earth's magnetotail observed with ARTEMIS, *J. Geophys. Res.*, *117*, A05231, doi:10.1029/2011JA017377.
Kiehas, S. A., V. Angelopoulos, A. Runov, and S.-S. Li (2013), On the azimuthal size of flux ropes near lunar orbit, *J. Geophys. Res. Space Physics*, *118*, 4415–4424, doi:10.1002/jgra.50425.
Lepping, R. P., J. A. Jones, and L. F. Burlaga (1990), Magnetic field structure of interplanetary magnetic clouds at 1 AU, *J. Geophys. Res.*, *95*(A8), 11,957–11,965.
Lindsay, S., M. James, E. Bunce, S. Imber, H. Korth, A. Martindale, and T. Yeoman (2016), MESSENGER X-ray observations of magnetosphere–surface interaction on the nightside of Mercury, *Planet. Space Sci.*, *125*, 72–79, doi:10.1016/j.pss.2016.03.005.
Lu, S., et al. (2015), Dipolarization fronts as earthward propagating flux ropes: A three-dimensional global hybrid simulation, *J. Geophys. Res. Space Physics*, *117*, A05231, doi:10.1002/2015JA021213.
Lundquist, S. (1950), Magnetohydrostatic Fields, *Ark. Fys.*, *2*, 361–365.
McPherron, R. L., B. C. T Russell, M. G. Kivelson, and P. J. Coleman (1973), Substorms in space: The correlation between ground and satellite observations of the magnetic field, *Radio Sci.*, *8*(11), 1059–1076.
Moldwin, M. B., and W. J. Hughes (1991), Plasmoids as magnetic flux ropes, *J. Geophys. Res.*, *96*(A8), 14,051–14,064, doi:10.1029/91JA01167.

Moldwin, M. B., and W. J. Hughes (1992), On the formation and evolution of plasmoids: A survey of ISEE 3 Geotail data, *J. Geophys. Res.*, *97*(A12), 19,259–19,282, doi:10.1029/92JA01598.
Ness, N., K. Behannon, R. Lepping, and Y. Whang (1976), Observations of Mercury's magnetic field, *Icarus*, *28*(4), 479–488, doi:10.1016/0019-1035(76)90121-4.
Ness, N. F., K. W. Behannon, R. P. Lepping, Y. C. Whang, and K. H. Schatten (1974), Magnetic field observations near mercury: Preliminary results from Mariner 10, *Science*, *185*(4146), 151–160.
Petrukovich, A. A. (2011), Origins of plasma sheet B_y, *J. Geophys. Res.*, *116*, A07217, doi:10.1029/2010JA016386.
Poh, G., J. A. Slavin, X. Jia, J. M. Raines, S. M. Imber, W.-J. Sun, D. J. Gershman, G. A. DiBraccio, K. J. Genestreti, and A. W. Smith (2017), Mercury's cross-tail current sheet: Structure, X-line location and stress balance, *Geophys. Res. Lett.*, *44*, 678–686, doi:10.1002/2016GL071612.
Priest, E. R. (1990), The equilibrium of magnetic flux ropes, *Geophys. Monogr.*, *58*, 1–22.
Richardson, I. G., S. W. H. Cowley, E. W. Hones, and S. J. Bame (1987), Plasmoid-associated energetic ion bursts in the deep geomagnetic tail: Properties of plasmoids and the postplasmoid plasma sheet, *J. Geophys. Res.*, *92*, 9997–10,013, doi:10.1029/JA092iA09p0999.
Rong, Z. J., A. T. Y. Lui, W. X. Wan, Y. Y. Yang, C. Shen, A. A. Petrukovich, Y. C. Zhang, T. L. Zhang, and Y. Wei (2015), Time delay of interplanetary magnetic field penetration into Earth's magnetotail, *J. Geophys. Res. Space Physics*, *120*, 3406–3414, doi:10.1002/2014JA020452.
Schindler, K. (1974), A theory of the substorm mechanism, *J. Geophys. Res.*, *79*(19), 2803–2810, doi:10.1029/JA079i019p02803.
Sibeck, D. G., G. L. Siscoe, J. A. Slavin, E. J. Smith, S. J. Bame, and F. L. Scarf (1984), Magnetotail flux ropes, *Geophys. Res. Lett.*, *11*(10), 1090–1093, doi:10.1029/GL011i010p01090.
Siscoe, G. L., N. F. Ness, and C. M. Yeates (1975), Substorms on Mercury?, *J. Geophys. Res.*, *80*(31), 4359–4363, doi:10.1029/JA080i031p04359.
Slavin, J. A., et al. (1989), CDAW 8 observations of plasmoid signatures in the geomagnetic tail: An assessment, *J. Geophys. Res.*, *94*(A11), 15,153–15,175, doi:10.1029/JA094iA11p15153.
Slavin, J. A., R. P. Lepping, J. Gjerloev, D. H. Fairfield, M. Hesse, C. J. Owen, M. B. Moldwin, T. Nagai, A. Ieda, and T. Mukai (2003), Geotail observations of magnetic flux ropes in the plasma sheet, *J. Geophys. Res.*, *108*, 1015, doi:10.1029/2002JA009557.
Slavin, J. A., E. I. Tanskanen, M. Hesse, C. J. Owen, M. W. Dunlop, S. Imber, E. A. Lucek, A. Balogh, and K. H. Glassmeier (2005), Cluster observations of traveling compression regions in the near-tail, *J. Geophys. Res.*, *110*, A06207, doi:10.1029/2004JA010878.
Slavin, J. A., et al. (2009), MESSENGER observations of magnetic reconnection in Mercury's magnetosphere, *SCIENCE*, *324*(5927), 606–610.
Slavin, J. A., et al. (2010), MESSENGER observations of extreme loading and unloading of Mercury's magnetic tail, *Science*, *329*(5992), 665–668, doi:10.1126/science.1188067.
Slavin, J. A., et al. (2012), MESSENGER and Mariner 10 flyby observations of magnetotail structure and dynamics at Mercury, *J. Geophys. Res.*, *117*, A01215, doi:10.1029/2011JA016900.
Slavin, J. A., et al. (2014), MESSENGER observations of Mercury's dayside magnetosphere under extreme solar wind conditions, *J. Geophys. Res. Space Physics*, *119*, 8087–8116, doi:10.1002/2014JA020319.
Smith, A. W., J. A. Slavin, C. M. Jackman, R. C. Fear, G.-K. Poh, G. A. DiBraccio, J. M. Jasinski, and L. Trenchi (2017), Automated force-free flux rope identification, *J. Geophys. Res. Space Physics*, *122*, 780–791, doi:10.1002/2016JA022994.
Solomon, S. C., R. L. McNutt Jr., R. E. Gold, and D. L. Domingue (2007), MESSENGER mission overview, *Space Sci. Rev.*, *131*(1–4), 3–39.
Sonnerup, B. U. Ö., and L. J. Cahill (1967), Magnetopause structure and attitude from Explorer 12 observations, *J. Geophys. Res.*, *72*(1), 171–183, doi:10.1029/JZ072i001p00171.
Sonnerup, B. U. Ö., and M. Scheible (1998), Minimum and maximum variance analysis, in *Analysis Methods for Multi-Spacecraft Data*, edited by G. Paschmann and P. W. Daly, pp. 185–220, ISSI Scientific Report SR-001, ISSI/ESA., Bern, Switzerland.
Sun, W.-J., et al. (2015), MESSENGER observations of magnetospheric substorm activity in Mercury's near magnetotail, *Geophys. Res. Lett.*, *42*, 3692–3699, doi:10.1002/2015GL064052.
Sun, W. J., S. Y. Fu, J. A. Slavin, J. M. Raines, Q. G. Zong, G. K. Poh, and T. H. Zurbuchen (2016), Spatial distribution of Mercury's flux ropes and reconnection fronts: MESSENGER observations, *J. Geophys. Res. Space Physics*, *121*, 7590–7607, doi:10.1002/2016JA022787.
Sundberg, T., et al. (2012), MESSENGER observations of dipolarization events in Mercury's magnetotail, *J. Geophys. Res.*, *117*, A00M03, doi:10.1029/2012JA017756.
Teh, W.-L., R. Nakamura, H. Karimabadi, W. Baumjohann, and T. L. Zhang (2014), Correlation of core field polarity of magnetotail flux ropes with the IMF B_y: Reconnection guide field dependency, *J. Geophys. Res. Space Physics*, *119*, 2933–2944, doi:10.1002/2013JA019454.
Tenfjord, P., N. Østgaard, K. Snekvik, K. M. Laundal, J. P. Reistad, S. Haaland, and S. E. Milan (2015), How the IMF B_y induces a B_y component in the closed magnetosphere and how it leads to asymmetric currents and convection patterns in the two hemispheres, *J. Geophys. Res. Space Physics*, *120*, 9368–9384, doi:10.1002/2015JA021579.
Vogt, M. F., M. G. Kivelson, K. K. Khurana, S. P. Joy, and R. J. Walker (2010), Reconnection and flows in the Jovian magnetotail as inferred from magnetometer observations, *J. Geophys. Res.*, *115*, A06219, doi:10.1029/2009JA015098.
Walsh, A. P., et al. (2014), Dawn dusk asymmetries in the coupled solar wind magnetosphere ionosphere system: A review, *Ann. Geophys.*, *32*(7), 705–737, doi:10.5194/angeo-32-705-2014.
Winslow, R. M., B. J. Anderson, C. L. Johnson, J. A. Slavin, H. Korth, M. E. Purucker, D. N. Baker, and S. C. Solomon (2013), Mercury's magnetopause and bow shock from MESSENGER Magnetometer observations, *J. Geophys. Res. Space Physics*, *118*, 2213–2227, doi:10.1002/jgra.50237.
Xiao, C. J., Z. Y. Pu, Z. W. Ma, S. Y. Fu, Z. Y. Huang, and Q. G. Zong (2004), Inferring of flux rope orientation with the minimum variance analysis technique, *J. Geophys. Res.*, *109*, A11218, doi:10.1029/2004JA010594.
Zhong, J., W. X. Wan, J. A. Slavin, Y. Wei, R. L. Lin, L. H. Chai, J. M. Raines, Z. J. Rong, and X. H. Han (2015), Mercury's three-dimensional asymmetric magnetopause, *J. Geophys. Res. Space Physics*, *120*, 7658–7671, doi:10.1002/2015JA021425.